A Simple Integrated and Low-Radiation Receiver for Inductive Power Transfer

Yiming Yin, Heyuan Li, *Graduate Student Member, IEEE*, Shiqi Gao, Yong Li, *Senior Member, IEEE*, Xian Zhang, *Member, IEEE*, and Minfan Fu, *Senior Member, IEEE*

***Abstract*—It is promising to pursue an integrated low-profile receiver (RX) for inductive power transfer applications. However, the existing integration solutions suffer from the complicated structure and the insertion of dielectric material. This article proposes a novel excitation approach for the classical three-layer RX, and the structure inductance and capacitance are utilized for self-resonance. Without using additional dielectric material, proper magnetic material is evaluated and selected toward enhancing the structure capacitance and reducing the dielectric losses. The circuit model, radiation performance, and structure optimization are discussed in the simulation and experiment. A 750-kHz 100-W system is demonstrated to have a 92.4% coupler efficiency and 87.5% system efficiency. Compared to a classical RX, the proposed RX would slightly improve the shielding effect for the magnetic field and dramatically reduce the electric-field radiation by 15 dBm.**

***Index Terms*—Inductive power transfer (IPT), integrated receiver (RX), low electric-field radiation, self-resonance.**

I. Introduction

INDUCTIVE power transfer (IPT) has shown its great capability in meeting various power demands without physical connections. The achieved spacial freedom and isolated design enable the device charging in a safe and convenient manner [1], [2]. These attractive features truly benefit lot of charging scenarios, including medical implants, wearables devices, moving robots, and electric vehicles [3], [4], [5]. A typical IPT system usually includes a transmitter (TX) and a receiver (RX) for electromagnetic coupling. When a wire-charged device is modified to enable wireless charging, the RX-side circuits (at least including the coil, RX compensation, and rectifier) need to be fully embedded. Compared to the TX, the RX has to consider more about its size constrain, which is particularly important for low- or medium-power devices. Therefore, it is meaningful to explore a low-profile integrated RX [6], [7].

It is well known that the size of power electronic converters is mainly affected by the switching frequency. In the past few years, the significant improvement of wide bandgap semiconductors and soft-switching techniques has successfully pushed the switching frequency to several hundreds of kHz and even several MHz. Such kind of improvement directly helps reduce the volume of passive components, such as capacitor, inductor, transformer, and coupler. All these achievements contribute to the next-generation power supplies for various classical power conversion areas [8], [9], [10]. An IPT system is also an isolated and varied-coupling resonant dc–dc converter. Besides the coupler, large amount of additional passive components need to be used for the compensation purposes. When high-frequency operation is employed, the PCB coil or copper-foil coil is able to be used with less turn numbers, and it would benefit the low-profile RX design [11].

In a typical IPT system, the most volume-sensitive component is the inductive coupler [12]. It is attractive to develop an integration solution for the coupler and compensation [13], [14], [15], [16]. A common solution is to utilize and enhance the mutual capacitance between different coil turns for self-resonance. When applying this concept in a single-layer coil, the gap of same-layer adjacent coil is used to build the required capacitance [17]. In order to reduce the self-resonant frequency, multilayer PCB coils are customized by inserting dielectric material to increase the structure capacitance [18], [19]. Due to the structure complexity, several structures require complicated distributed circuit models to explain the resonances [20], [21], [22]. Different to the modification of classical coil, another effective integration solution is to customize the bifilar coil [23], [24], which offers more options for the connection between coil and external circuits. In [25], planar open-ended bifilar coils are used to form series resonance. Besides, double-layer short-ended bifilar coils serve to create parallel resonance [26]. The self-resonant coil would also consider the shielding layer design for lower radiation [27]. All the abovementioned approaches (i.e., using either classical coils or bifilar coils) need to modify the existing coil structure, and dielectric material is usually needed to enhance the capacitance for lowering the self-resonance frequency. Considering

Manuscript received 28 December 2022; revised 26 February 2023 and 29 April 2023; accepted 19 May 2023. Date of publication 26 May 2023; date of current version 1 September 2023. This work was supported in part by the National Natural Science Foundation of China under Grants 51977147 and 52007120 and in part by the National Science Fund for Excellent Young Scholars under Grant 52122701. Recommended for publication by Associate Editor F. Lu. *(Corresponding author: Minfan Fu.)*

Yiming Yin, Heyuan Li, and Shiqi Gao are with the School of Information Science and Technology, ShanghaiTech University, Shanghai 201210, China (e-mail: yinym@shanghaitech.edu.cn; lihy4@shanghaitech.edu.cn; gaoshq@shanghaitech.edu.cn).

Yong Li is with the School of Electrical Engineering, Southwest Jiaotong University, Chengdu 611756, China (e-mail: yong_li@swjtu.edu.cn).

Xian Zhang is with the School of Electrical Engineering, Hebei University of Technology, Tianjin 300130, China (e-mail: zhangxian@hebut.edu.cn).

Minfan Fu is with the School of Information Science and Technology, ShanghaiTech University, Shanghai 201210, China, and also with the Shanghai Engineering Research Center of Energy Efficient and Custom AI IC, Shanghai 201210, China (e-mail: fumf@shanghaitech.edu.cn).

Color versions of one or more figures in this article are available at https://doi.org/10.1109/TPEL.2023.3280194.

Digital Object Identifier 10.1109/TPEL.2023.3280194

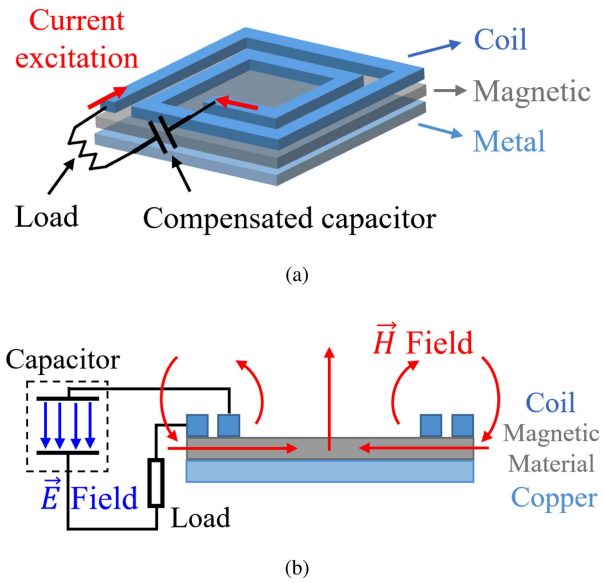

Fig. 1. Classical RX. (a) Physical structure. (b) Field distribution.

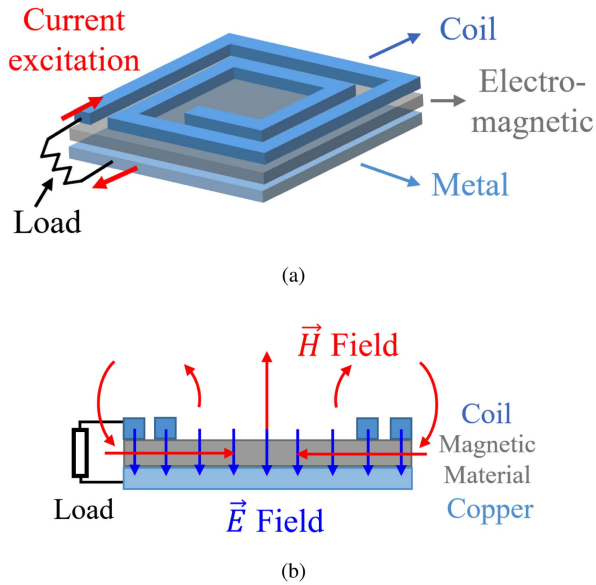

Fig. 2. New RX. (a) Physical structure. (b) Field distribution.

the fabrication challenges, the structure complexity makes it difficult for the moving from a laboratory system to a practical application.

This article proposes a novel integration concept by changing the excitation method instead of modifying the classical structure. A classical RX usually includes a coil layer, a magnetic layer, and a shielding layer. The proposed RX would use both the coil layer and the shielding layer as the excitation terminals. Such a circuit would be equivalently studied as a series resonant tank. Without using dielectric material, the middle magnetic material needs to deal with both magnetic and electric field. This article would evaluate the dielectric parameters for the existing magnetic material, and a circuit-model-based parameter extraction is used to select promising material. The radiation performance of the new RX is compared with the classical one. The RX structure optimization is briefly discussed in the experiment. When powered by a traditional TX, the new-RX-based system is able to achieve high-efficiency performance for high-voltage low-current application with dramatic reduction in electric-field radiation. This simple integration approach would truly benefit the fabrication and mass production.

II. Integrated RX Using Shielding Layers

A. RX Structure

An RX is responsible for utilizing the magnetic flux from the TX. At high frequency, the PCB winding or copper foil would benefit a low-profile design. A classical RX is shown in Fig. 1(a), which is a typical three-layer structure. At the top layer, the planar coil would receive the magnetic flux from the TX side; the middle layer is a magnetic plate to guide the magnetic flux and enhance the coupling; a conductive metal plate would be added to the bottom to reduce the radiation. In order to fully utilize the induced voltage at the RX coil, additional compensations (such as the series capacitor) are needed to reduce the circulating energy, and help the load get sufficient power. For the example series compensation, the resonance of RX means the energy exchange between the coil inductor (i.e., the energy of magnetic field) and the compensation capacitor (i.e., the energy of electric field). Fig. 1(b) gives the field distribution of the classical RX. It is clear that the electric field is strongly confined within the external capacitor, and that the magnetic field is mainly around the coil. There is no space overlapping between two types of field.

This article is trying the explore a novel integration concept by confining both types of field in the same space. As shown of Fig. 2(a), the proposed RX structure is almost the same as the original one of Fig. 1(a). In the original structure, the two terminals of the coil are connected to the load-side circuits. The new RX only has one coil terminal connected and the other floated. Instead, the metal layer is used as the current returning loop. It means the original structure is excited by a different manner. Through this modification, the external series capacitor is no longer needed due to the structure capacitance between the coil layer and shielding layer. The field distribution is shown in Fig. 2(b). Both types of field are confined around the RX.

B. Circuit Model of Integrated RX

The equivalent circuit model is needed to study the resonance behavior and guide the structure optimization. Using the new excitation approach, the RX structure model is simplified as shown in Fig. 3(a). It is clear that the distributed model is needed if the wide-frequency characteristics are evaluated. A more accurate circuit model may use the transmission line theory to explore the influence of the size parameters on a wider frequency range. However, the complicated internal coupling and fringing effect could accurately calculate but complicate the model [28]. Fortunately, the RX response at the self-resonance frequency f_{rx} (i.e., the operation frequency) is sufficient to

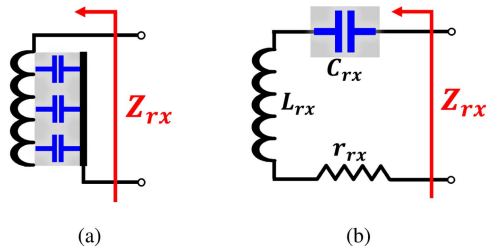

Fig. 3. Circuit model of proposed integrated RX. (a) Distributed circuit model. (b) Lumped circuit model.

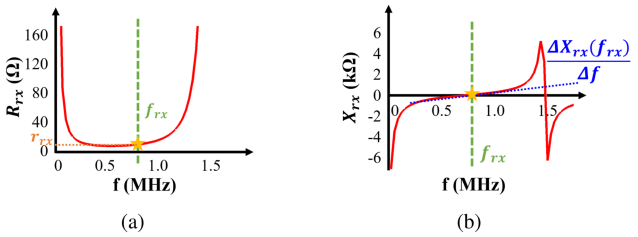

Fig. 4. Input impedance of a sample RX. (a) Real part: $R_{\rm rx}$. (b) Imaginary part: $X_{\rm rx}$.

evaluate the power and efficiency characteristics. Therefore, a series resonant tank using lumped components is used to model the new RX. In Fig. 3(b), $L_{\rm rx}$, $C_{\rm rx}$, and $r_{\rm rx}$ are the equivalent series inductance (ESL), equivalent series capacitance (ESC), and equivalent series resistance (ESR) at $f_{\rm rx}$. The self-resonance between the ESL and ESC is set as the excitation frequency or the switching frequency f_s. The quality factor of the whole RX is defined as $Q_{\rm rx} = \frac{2\pi f_{\rm rx} L_{\rm rx}}{r_{\rm rx}}$.

In order to extract the model parameters, a real RX sample is fabricated and its wide-frequency input impedance ($\boldsymbol{Z}_{\rm rx}(f) = R_{\rm rx}(f) + jX_{\rm rx}(f)$) is measured in Fig. 4. Its real part $R_{\rm rx}$ at $f_{\rm rx}$, i.e., $R_{\rm rx}(f_{\rm rx})$, equals to the RX ESR (i.e., $r_{\rm rx}$) [refer to Fig. 4(a)]. In Fig. 4(b), the first cross-zero point (i.e., zero reactance, $X_{\rm rx}(f_{\rm rx})) = 0$) indicates the self-resonance frequency $f_{\rm rx}$, and the curve slope of $X_{\rm rx}$ around $f_{\rm rx}$ are determined by the resonant components ($L_{\rm rx}$ and $C_{\rm rx}$). Therefore, it has

$$\begin{cases} R_{\rm rx}(f_{\rm rx}) = r_{\rm rx} \\ X_{\rm rx}(f_{\rm rx}) = 2\pi f_{\rm rx} L_{\rm rx} - 1/(2\pi f_{\rm rx} C_{\rm rx}) = 0 \\ 2\pi L_{\rm rx} + 1/(2\pi f^2 C_{\rm rx}) = \Delta X_{\rm rx}(f)/(\Delta f). \end{cases} \tag{1}$$

In Fig. 4, it is clear that the *RLC* model is not able to describe the all the frequency characteristics. At higher frequency, another parallel resonance frequency also exists. The using of RLC model actually means a tradeoff between the model simplicity and accuracy. Based on this model, the impedance (measured by impedance analyzer) is sufficient to extract the RX circuit parameters for the new RX.

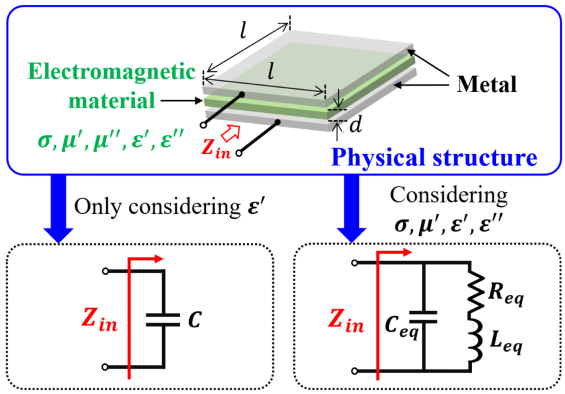

Fig. 5. Physical structure for material parameter extraction.

III. Parameter Extraction and Selection of Electromagnetic Material

A. Review of Electromagnetic Material

In the proposed structure, the middle layer (i.e., the magnetic layer) needs to deal with both types of field. This general electromagnetic material has to consider the following five parameters: conductivity (σ), complex permittivity ($\boldsymbol{\varepsilon} = \varepsilon' + j\varepsilon''$), and complex permeability ($\boldsymbol{\mu} = \mu' + j\mu''$). Here, σ, ε'', and μ'' are related to the conduction loss P_C, E-field-related loss P_E, and H-field-related loss P_H, respectively. The electromagnetic parameters should benefit the energy exchange between the magnetic field and electric field. Instead of randomly searching for a describable material, this article tries to evaluate the existing magnetic material with good dielectric parameters $\boldsymbol{\varepsilon}$, i.e., high ε' and low ε''.

In the classical RX structure, the magnetic layer is used to enhance the coupling and guide the magnetic flux at the resonance frequency f_s. Since both μ' and μ'' are frequency dependent, the magnetic material should have sufficient μ' to enhance the field and ignorable μ'' to avoid high P_H at f_s. Meanwhile, in order to minimize the high-frequency ($>> f_s$) magnetic-field radiation, a large μ'' is preferred. The proposed RX should still follow this rule to select the material candidate around f_s (about several MHz), which indicates that $\mu''(f_s) \approx 0$. Usually the material manufacturer is able to provide $\boldsymbol{\mu}$ for magnetic material, but $\boldsymbol{\varepsilon}$ is unknown. Therefore, this article has to evaluate and measure $\boldsymbol{\varepsilon}$ for the various candidates.

B. Circuit-Model-Based $\boldsymbol{\varepsilon}$ Extraction

The basic idea for extracting $\boldsymbol{\varepsilon}$ is to use a well-known structure with clear circuit model. By measuring circuit parameters, the material parameters are calculated. As shown in Fig. 5, a three-layer structure is built with the candidate material inserting as the middle layer. Both the top and bottom layer are copper plates. All the three layers have the same width and length, i.e., l. The thickness of the middle layer is d. In order to minimize the fringing effect, it needs $l >> d$, which dramatically simplifies the circuit model. It is more convenient to extract the material parameter. When an ideal dielectric material is used, i.e., only

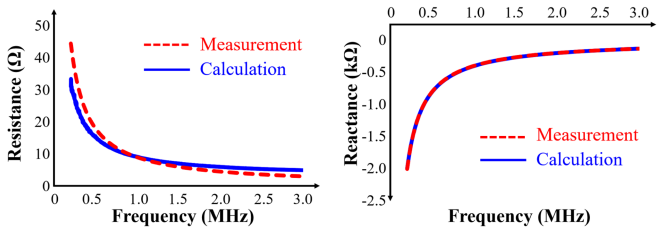

(a) (b)

Fig. 6. Circuit parameters extraction. (a) Resistance. (b) Reactance.

considering the effect of ε', this structure would build a classical capacitor with capacitance equals to $C = \frac{\varepsilon' l^2}{d}$.

In this article, when the candidate magnetic material is inserted as the middle layer, ε' and ε'' are unknown. Note that σ and μ' are provided by the manufacturer and $\mu'' \approx 0$. The task is to extract two independent parameters. When the structure of Fig. 5 needs to consider the effect of σ, μ', ε', and ε'', the single-capacitor model is no longer valid. According to [29], the equivalent circuit model of this structure could be represented as a parallel *RLC* branch in Fig. 5. The circuit parameters could be derived based on the material parameter as follows:

$$\begin{cases} L_{\text{eq}} = \mu' d/3 \\ C_{\text{eq}} = \varepsilon' l^2/d \\ R_{\text{eq}} = d/[(\sigma + 2\pi f_s \varepsilon'') l^2]. \end{cases} \tag{2}$$

Therefore, measuring the abovementioned three circuit parameters would help obtain the target material parameters, i.e., ε', and ε''.

Such kind of parameter extraction needs to measure a real structure. For example, when a material candidate is used, the input impedance $\boldsymbol{Z}_{\text{in}}$ $(= R_{\text{in}} + jX_{\text{in}})$ could be measured by the impedance analyzer around f_s. Based on the *RLC* model of Fig. 5, it has

$$\begin{cases} R_{\text{in}} = \frac{R_{\text{eq}}}{(1-4\pi^2 f_s^2 L_{\text{eq}} C_{\text{eq}})^2 - 4\pi^2 f_s^2 R_{\text{eq}}^2 C_{\text{eq}}^2} \\ X_{\text{in}} = \frac{2\pi f_s (L_{\text{eq}} - R_{\text{eq}}^2 C_{\text{eq}} - 4\pi^2 f_s^2 L_{\text{eq}}^2 C_{\text{eq}})}{(1-4\pi^2 f_s^2 L_{\text{eq}} C_{\text{eq}})^2 - 4\pi^2 f_s^2 R_{\text{eq}}^2 C_{\text{eq}}^2}. \end{cases} \tag{3}$$

Combining (3) and (2), the measured R_{in} and X_{in} are sufficient to calculate the unknown ε', and ε''. Please note that the lumped *RLC* model is not able to describe the wide-frequency characteristics. All the material parameters are in-theory frequency dependent. In this article, it is sufficient to use the material parameters around f_s to study the efficiency and power characteristics of RX.

C. Case Study and Material Selection

TDK IBF15 is used as a study case for material parameter extraction. A real structure of Fig. 5 is fabricated with the material sample. A impedance analyzer is used to measure the input impedance, i.e., a one-port network when the conductive plates serve as terminals. Both the measured resistance and reactance are shown in Fig. 6. A *RLC* model (i.e., the red dot line) is able to fit the measured curve for a short frequency range (around the target f_s). Based on the impedance information, the

TABLE I
PARAMETERS OF TDK IBF15

Measured results	Size [mm]	f [MHz]	R_{in} [Ω]	X_{in} [Ω]
	125×125×1.2	1	9.01	–410.02
Extracted paramters	σ [S/m]	ε' [F/m]	ε'' [F/m]	μ' [H/m]
	10^{-9}	$3.4\varepsilon_0$	$0.075\varepsilon_0$	$130\mu_0$

TABLE II
PARAMETERS COMPARISON OF CANDIDATE MATERIALS

Candidate	σ [S/m]	ε' [F/m]	ε'' [F/m]	μ' [H/m]
TDK IBF15	1×10^{-9}	$3.4\varepsilon_0$	$0.075\varepsilon_0$	$130\mu_0$
TDG TRF220	1×10^{-9}	$4.05\varepsilon_0$	$0.102\varepsilon_0$	$170\mu_0$
TDG TN200B	1×10^{-9}	$1.46\varepsilon_0$	$0.027\varepsilon_0$	$2000\mu_0$
WSDS P600	1×10^{-7}	$1.41\varepsilon_0$	$0.018\varepsilon_0$	$150\mu_0$
WSDS P15	1.5×10^{-6}	$7.46\varepsilon_0$	$0.050\varepsilon_0$	$197\mu_0$

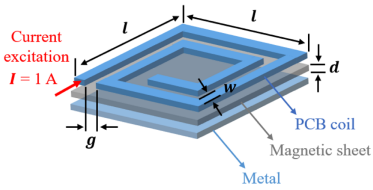

Variables	Values
Turns N	16
Size Length l	10 cm
Coil Line Gap g	0.6 mm
Coil Line Width w	1.0 mm
Material Thickness d	1.5 mm
Current Excitation I	1 A

Fig. 7. RX layout in HFSS.

circuit parameters and material parameters are given in Table I with the help of (2) and (3), where ε_0 and μ_0 represent the vacuum permittivity and vacuum permeability.

When the different material is used in Fig. 5, the proposed parameter extraction approach is applied, and five types of material are evaluated and compared in Table II. In the integrated RX, the capacitance is mainly contributed by ε' when the size is fixed. Therefore, a high ε' is preferred to build a large capacitance, which helps lower the self-resonance frequency. From the loss point of view, low ε'' is preferred to reduce E-field-related losses. Considering these demands for ε' and ε'', WSDS P15 is finally selected. When this material is inserted in Fig. 2, a typical three layer structure is formed. The material conductivity means a high resistivity (about 10^9), and no more insulation layer is needed inside the RX.

IV. RADIATION PERFORMANCE

A. Simulation Setup

In the classical RX of Fig. 1, the function of each layer is clear: the coil layer captures the flux; the magnetic layer guides the flux; and the copper layer shields the leakage flux. In the new RX of Fig. 2, although the basic structure does not change, the excitation terminal change will affect the shielding effects. In order to evaluate the radiation effect, an RX is built, as shown in Fig. 7. This RX would be excited with both the classical and the

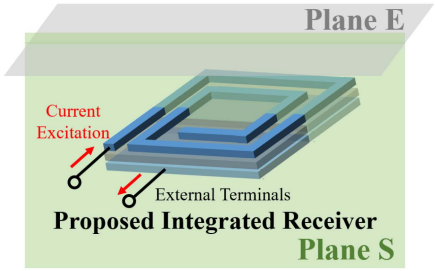

Fig. 8. Current excitation setup and planes for field evaluation.

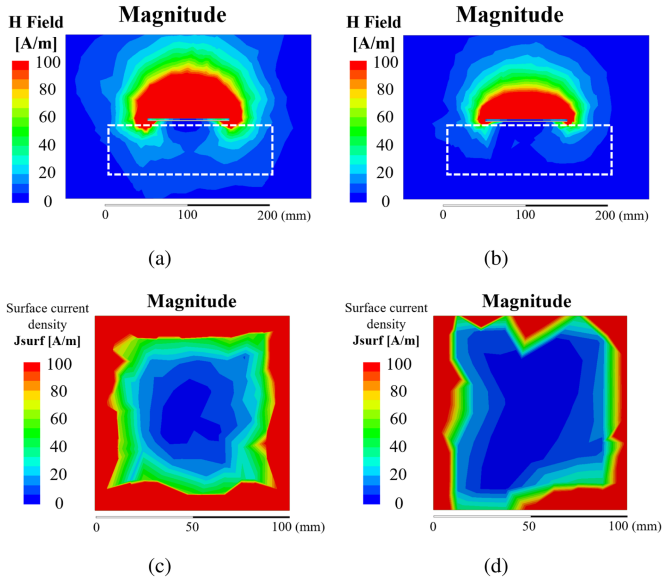

Fig. 9. Magnetic-field and current distribution. (a) H field of the classical RX. (b) H field of the proposed RX. (c) Current density of the classical RX. (d) Current density of the proposed RX.

proposed approaches. The finite element analysis (FEA) simulation (i.e., HFSS in this article) is used for radiation comparison.

As shown in Fig. 7, the length of the square RX is l (=10 cm). In order to have a small RX, i.e., using less turns of coils, a larger structural capacitance is preferred, which is determined by the thickness of the middle layer. In this article, a 1.5-mm material layer is used, which is thinnest sample from the manufactures. In the coil layer, it is a PCB coil with 16 turns, 0.6-mm turn gap, and 1.0-mm line width. These PCB parameters could be optimized toward benefiting the efficiency from the circuit point of view. Here, the setup is just used to compare two RXs with different excitation terminals. For both types of RX, a 1-A excitation current is used in the simulation. As shown in Fig. 8, the cross-section plane of Plane S would serve to observe the field distribution.

B. Magnetic-Field Distribution

Fig. 9 compares the magnetic-field distribution. The coil layer is placed on the top and the bottom layer is used for shielding. Therefore, the field of bottom area (within the white dot block) represents the magnetic-field radiation. Both the classical RX and the proposed one show to have effective shielding effect.

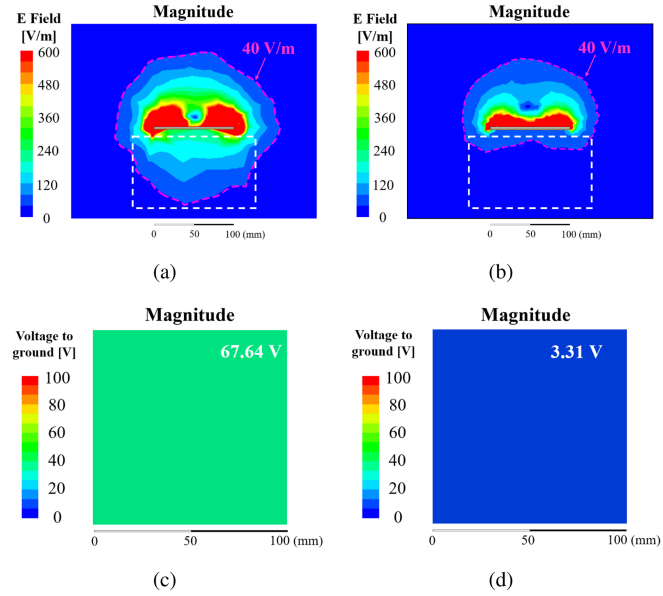

Fig. 10. Electric-field and -voltage distribution. (a) E field of the classical RX. (b) E field of the proposed RX. (c) Voltage of the metal plate in the classical RX. (d) Voltage of the metal plate in the proposed RX.

In Fig. 9(a), it is straightforward to explain low magnetic-field radiation of the classical RX. Magnetic material would guide the center flux to the edge and then back to the upper area. The rest leakage flux will be eliminated by the bottom metal layer. Fig. 9(b) shows the proposed RX would slightly lower the radiation when the RXs have the same current. In order to explain this effect, it is necessary to understand the current distribution of the coil. As shown in Fig. 1(a), when the input current is fixed, each turns of the coil would have the same current. For the proposed RX, the distributed current would flow through the structure capacitance to the bottom layer. As a result, the current of the inner turn is smaller than that of the outer turn. When the loop current of each turn contributes to the final magnetic field, the proposed RX would naturally has smaller radiation. Another factor affecting the leakage H field is the current density of the bottom metal plate, which is compared in Fig. 9(c) and (d). For both RXs, the center has a lower current while the edge has a higher current. It is clear that the proposed RX has a smaller current density, which is consistent with the field distribution of Fig. 9(a) and (b).

C. Electric-Field Distribution

In the far-field area, the correlation between the H field and E field is clear and the wave impedance is constant (377 Ω) in free space. There is no need to study them in a separated manner. However, the near-field coupler would have quite different conclusions. The proposed excitation would lead a quite different electric-field distribution. The electric-field shielding effect cannot be simply indicated by the abovementioned discussion for magnetic field. Based on the FEA simulation in HFSS, the electric-field distribution are recorded and compared in Fig. 10(a) and (b). The field distribution of different RXs are

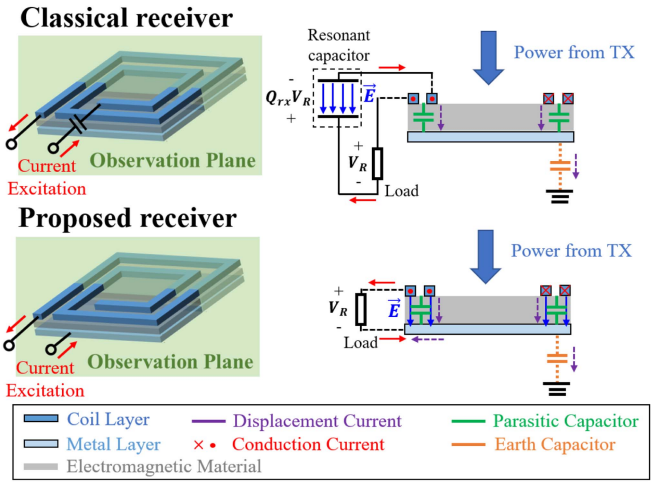

Fig. 11. Structure terminal voltage for different RXs.

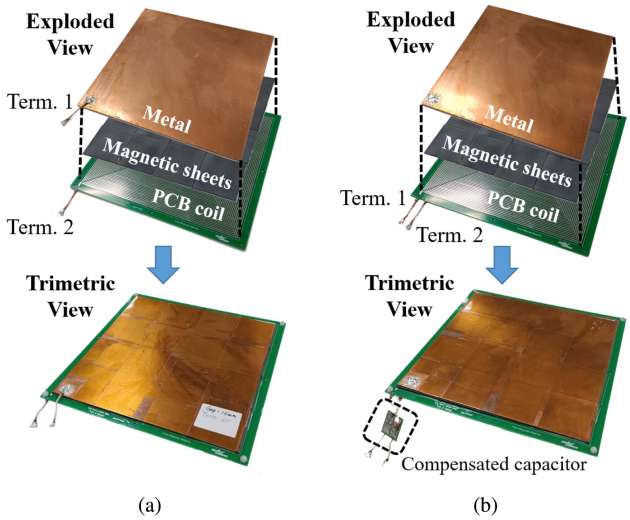

Fig. 12. Real RX structure. (a) Proposed RX. (b) Classical RX.

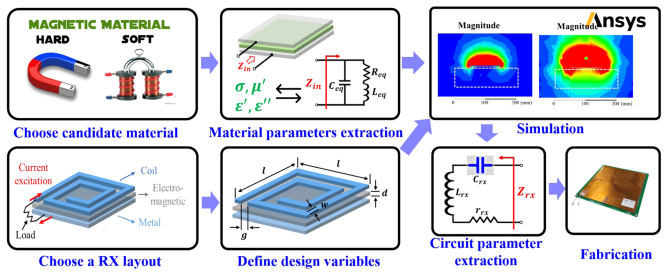

Fig. 13. Design flow chart.

almost the same in the upper area due to the power transfer. However, in the bottom area, electric-field radiation of the proposed RX is much lower than that of classical one. According to the standard of GB 8702-2014, the maximum electric field for a living body should be smaller than 40 V/m. Therefore, a pink dot line is used in Fig. 10(a) and (b) to enclose the high-radiation region, which is helpful to quantitatively justify the E-field leakage reduction.The following part would use the structure and excitation to explain this observation.

It is known the electrical field radiation of an object is caused by its voltage, referring to the Earth ground. When the bottom area of Fig. 10(a) shows higher radiation, it means a higher floating voltage exists for the classical RX. As shown in Fig. 10(c) and (d), the voltage magnitude of the metal plate is compared for both RXs. It is clearly that the metal layer of the classical RX would be induced with a much higher floating voltage. When the metal plate of the proposed RX is used as the returning loop, the floating voltage would be dramatically reduced. The E-field reduction could also be explained from the terminal excitation. As shown in In Fig. 11, the load voltage magnitude is V_R for both RXs. Under resonance, the resonant voltage of the external capacitor is $Q_{\rm rx}V_R$. In the classical RX of Fig. 11, the terminal voltage is $(Q_{\rm rx}+1)V_R$, and $Q_{\rm rx}>>1$. In the new RX of Fig. 11, the electrical field for resonance is also confined with the structure, and the excitation thermal voltage is V_R. Due to the dramatic reduction in the termination voltage, the proposed RX would significantly reduce the electric-field radiation. In the prior papers, most of the radiation study only consider the magnetic field, and it is due to the target application has high current and low voltage. Since the proposed RX is able to dramatically reduce the E-field radiation, the proposed RX would have clear benefits for high-voltage low-current application. Note that a high voltage naturally lead to higher radiation in a classical RX.

V. Experimental Verification

A. RX Fabrication

In this article, the RX is optimized toward to have a high-quality factor at the target frequency (about 1 MHz). An example square RX is used to evaluate the influence of the design variables. As shown in Fig. 12(a), the length of the square RX is 20-cm length. Each sample RX is fabricated by tightly attaching three layers, i.e., the copper layer, the material layer, and the PCB layer. Note that the PCB coil is made by rude copper and its copper surface is directly facing the magnetic layer. The base material of the PCB (i.e., FR4 layer) will not affect the circuit parameters and radiation performance of RX. The classical RX in Fig. 12(b) only changes the excitation approach and requires additional compensation. In practice, both RXs of Fig. 12 still need additional insulation to ensure human-touch safety for the regulation [30]. It would also avoid the conductive interference for the data communication.

Given a structure of Fig. 7 and the material parameters for the middle layer, the FEA-based analysis is able to simulate the RX and helps derive the RX circuit parameters. The simulation-based design flow chart is shown in Fig. 13. The key point is to choose the design variables without causing fabrication troubles. It is known that the capacitance is mainly contributed by the overlapping of two conductive layers. Since the middle magnetic layer is not able to offer larger ε' as the common dielectric material, the thickness of the middle layer should be small enough to ensure large structure capacitance, which may help have a lower self-resonance frequency. According to the fabrication limitation of the material manufactures, thinnest material thickness d is 1.5 mm. In such a three-layer structure,

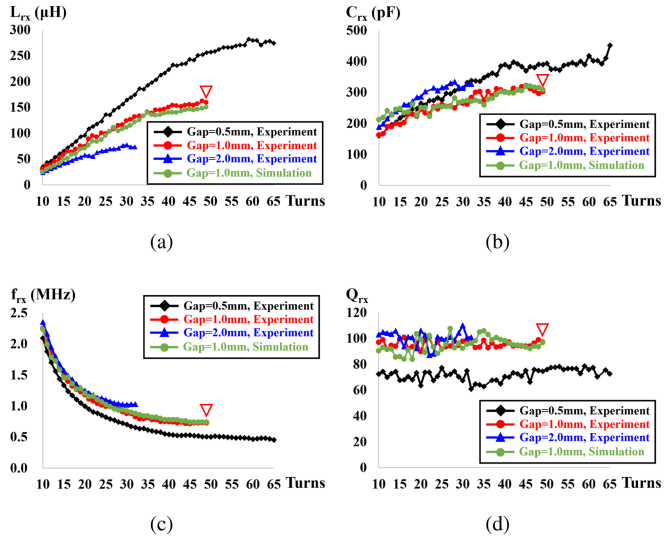

Fig. 14. Influence of RX size parameters. (a) Inductance: L_{rx}. (b) Capacitance: C_{rx}. (c) Self-resonance frequency: f_{rx}. (d) Quality factor: Q_{rx}.

the major design variables are provided by the PCB coil, such as the line width w, gap g, and turns number N (refer to Fig. 7). For convenience, w is fixed at 1.0 mm, and the influence of g and N are evaluated.

B. RX Parameter Measurement and Optimization

The influences of RX size parameters (g and N) are evaluated with the help of different RX samples. The impedance analyzer is used to measure the impedance of each sample, and the circuit parameters are extracted according to (1). The RX parameters are compared in Fig. 14. Three typical gaps ($g = 0.5$ mm, 1 mm, and 2 mm) are evaluated. Since the coil width is fixed, when different g is used, the maximum turn number is different, which means the coil fully covers the PCB surface. Fig. 14(a) shows the RX inductance would increase with N. This trend is similar to that of a classical RX. In Fig. 14(b), the RX capacitance also increases with N. As a result, the self-resonance frequency would decrease with N in Fig. 14(c). Based on the first three sub-figures, it is clear an RX with more turns and less gap is helpful to reduce the self-resonance frequency, which would benefit the active inverter and rectifier. The RX quality factor Q_{rx} is calculated based on the measured L_{rx} and r_{rx} and is shown in Fig. 14(d). Q_{rx} is mainly affected by g and shown to be relatively stable for different N. The RX is also conveniently designed with the help of FEA-based simulation. The simulation result for 1-mm gap is given in Fig. 14, i.e., the green line, which is consistent with the red curve. The final design point (i.e., ∇ in Fig. 14) actually make a tradeoff between Q_{rx} and f_{rx}, whose layout parameters are given in Table III.

C. Peak Efficiency

A new-RX-based IPT system is built to evaluate the overall dc–dc performance. The TX follows a classical design, which uses litz-wire to implement a circular coil (20-cm diameter)

TABLE III
PARAMETERS OF THE SELECTED COIL LAYER

Variables	Turns N	Size length l	Line gap g	Line width w
Values	49	20 cm	1.0 mm	1.0 mm

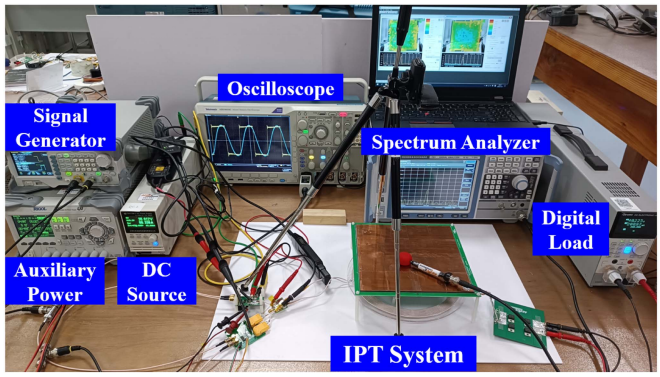

Fig. 15. Experiment setup for efficiency and radiation.

TABLE IV
CIRCUIT PARAMETERS OF EXPERIMENT SETUP

	Inductance L [μH]	Resistance r [Ω]	Quality factor Q	Capacitance C [pF]
TX Side	41.17	0.62	311.18	1081.69
Proposed RX Side	159.06	11.56	56.03	302.14
Classical RX Side	159.23	10.41	72.45	279.67
System Parameters	Frequency f_s [kHz]	Mutual inductor M [μH]	Distance [cm]	Coupling factor k
Values	754.2	18.86	5	0.23

and series compensation is applied. A test platform is built in Fig. 15, and all the system parameters given in Table IV. The measurement of the coupling coefficient k is similar to a classical system. When both sides work under resonant state, a current is injected to the TX coil, and the RX needs to measure the open circuit voltage. Under resonance, this voltage represents the induced voltage source of the coil and would help calculate the mutual inductance. Meanwhile, a classical RX (a PCB coil having same inductance) with external capacitors is added as a benchmark and the corresponding circuit parameters are also given in Table IV.

The circuit model of the demonstrated system is identical to a typical S-S IPT system. Therefore, several typical features are used to evaluate the power transfer characteristics. For example, once the coupler parameters are measured, the optimal load exists to optimize the coupler efficiency based on the following

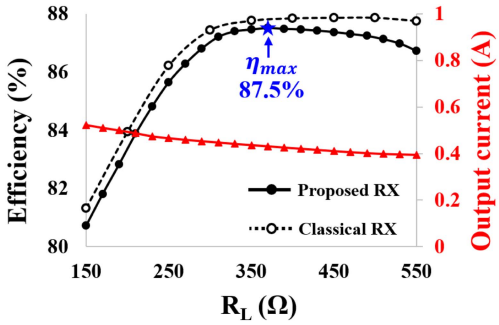

Fig. 16. IPT system efficiency and output current for different power level.

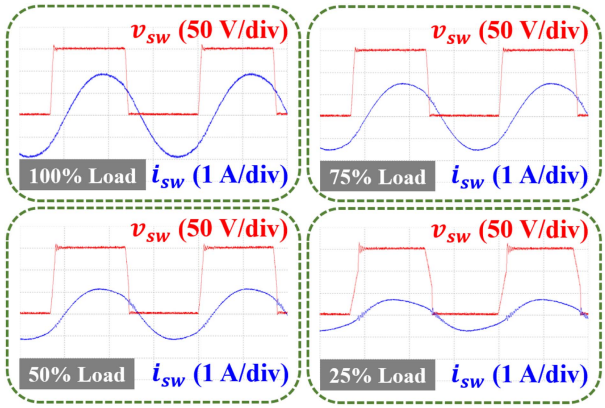

Fig. 17. Inverter output waveform at different power with 100%, 75%, 50%, and 25% load.

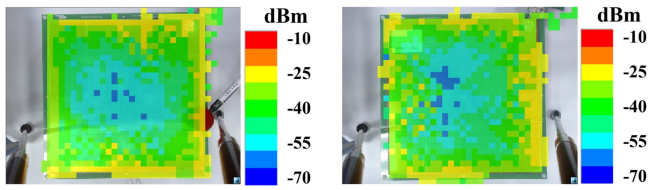

(a) (b)

Fig. 18. Magnetic-field distribution. (a) Classical RX. (b) Proposed RX.

well-known equations:

$$\begin{cases} \eta = \dfrac{4\pi^2 f_s^2 M^2}{r_{\rm tx} R_L + \frac{r_{\rm rx}(r_{\rm tx} r_{\rm rx} + 4\pi^2 f_s^2 M^2)}{R_L} + 4\pi^2 f_s^2 M^2 + 2 r_{\rm tx} r_{\rm rx}} \\ \eta_{\rm opt} = \dfrac{4\pi^2 f_s^2 M^2}{(\sqrt{4\pi^2 f_s^2 M^2 + r_{\rm tx} r_{\rm rx}} + \sqrt{r_{\rm tx} r_{\rm rx}})^2} \\ R_{L,\rm opt} = \sqrt{\dfrac{r_{\rm rx}(4\pi^2 f_s^2 M^2 + r_{\rm tx} r_{\rm rx})}{r_{\rm tx}}}. \end{cases} \tag{4}$$

Based on abovementioned equations and Table IV, the optimal ac resistor is calculated as 382 Ω, which in-theory leads to a 94.1% peak coupler efficiency. In order to measure the real coupler efficiency, the two-port scattering parameters are measured by the vector network analyzer. According to [31], these parameters would be used to calculate the coupler efficiency at small-signal level. The measured peak efficiency is 92.4%, which is close to the circuit-model-based estimation. Since the optimal load is at about several hundreds of Ω, the proposed RX is attractive for the application with high output voltage and low current.

A system-level evaluation is further carried out to test the dc to dc performance. A high-frequency half-bridge inverter (using GaN HEMT GS66508B) and a full-bridge rectifier (using Schottky diodes ASD465 A) are built to complete the IPT system. The overall dc–dc efficiency is measured through power analyzer (Yokogawa WT1802E). When the inverter is used, the TX input impedance should be tuned to slightly inductive to ensure zero-voltage switching (ZVS). When the input voltage is fixed, the whole system work exactly as an S-S IPT system and load-independent output current is achieved in Fig. 16. The peak efficiency is about 87.5%. The location of the peak efficiency point is consistent with the derived optimal load resistance. Compared to the benchmark system using a classical RX, the overall system efficiency using integrated RX would be lower due to decreased quality factor. Note that the ESR of the proposed RX would increase when the magnetic material is used as the dielectric one. At different power, the waveforms of inverter output are shown in the Fig. 17. The ZVS operation is ensured like a classical system.

D. Radiation Measurement

A space-electromagnetic-field visualization system (EPS-02Ev3, NoiseKen Inc.) is used to measure the field distribution as shown in Fig. 15. Using a spectrum analyzer (FSV7, Rohde&Schwarz Inc.), the magnetic and electric-field probes are able to measure the field magnitude at any position above the RX metal layer. At the same time, the top camera is able to detect the position of the colored probe. The PC would combine the field and position information to generate a field-distribution map.

In Fig. 8, the cross-section Plane S serves the best observation plane for field evaluation. It is easy to define the plane and obtain the field in simulation. However, the real system is not allowed us to carry out the same test by inserting the probes without affecting the system operation. Therefore, another horizontal Plane E in Fig. 8 is selected for field measurement, which is right above the metal layer of the RX. A classical RX serves as the benchmark for field comparison [refer to Fig. 12(b)]. Both systems would employ the same inverter, rectifier, working frequency, TX-side coil, and TX-side compensation. Since the current of the RX is the source of radiation, the primary excitation is tuned to ensure the same output current (using 200 mA) at the same load resistance.

The measured magnetic field is compared in Fig. 18. The color bar is used to mark the field intensity. In this test, the magnitude of magnetic field is about −45 dBm for both systems. The H-field radiation of proposed RX is slightly better, which is in consistent with the simulation results.

In order to justify the low-E radiation and its mechanism, Fig. 19(a) and (b) show the simulated voltage of the metal plate for the different RXs. In the simulation, a large boundary box is used to enclose the RX and treated as the Earth ground, and the real current is injected into the RX terminals. The

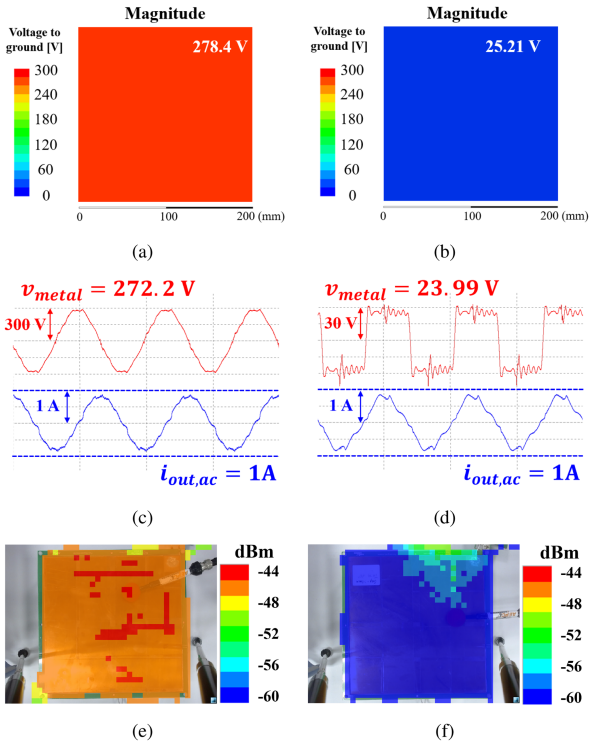

Fig. 19. Electric-field-related performance comparison. (a) Floating voltage of the classical RX in simulation. (b) Floating voltage of the proposed RX in simulation. (c) Measured voltage of the classical RX. (d) Measured voltage of the proposed RX. (e) Measured electric-field distribution of the classical RX. (f) Measured electric-field distribution of the proposed RX.

simulation results show the floating voltage reduction for the new RX. Then, the floating voltage is measured by a voltage probe and shown in Fig. 19(c) and (d). This voltage has the same frequency as the current and its magnitude is consistent with the simulated result. Finally, Fig. 19(e) and (f) compare the measured electric-field distribution. In terms of the intensity of electric field, the proposed RX shows 15 dBm lower than the classical one. Since the E-field radiation is closed related to the terminal voltage, when the proposed RX is used for high-voltage low-current application, its benefit would become more attractive.

The low-E radiation and the large optimal load resistance mean the proposed RX is attractive for high-voltage low-current application. When the proposed RX is introduced for high power application, it needs to consider the current and voltage rating. For example, the PCB coil needs to carry higher current, and the middle material needs to ensure insulation under high terminal voltage. Generally, a high-frequency self-resonance coil is not suitable for high power. One appealing application for the proposed RX is the medical implant charging. This application has low-power demand, large load resistance, strict size constrains, and low-radiation requirement.

VI. Conclusion

This article explores the potential of confining the magnetic field and electric field within a classical RX structure without inserting dielectric material. A simple integration approach is proposed by directly changing the excitation of the classical RX. Its internal field distribution and equivalent circuit model are discussed. When dealing with both types of field, the existing high-frequency magnetic material is evaluated in terms of its parameter for electric field. The RX shielding effects are evaluated with the help of simulation. A square RX sample is briefly evaluated and optimized in the experiment. Using the proposed RX, the peak coupler efficiency is 92.1% and the system efficiency is 87.5%. Compared to a classical RX, the proposed RX is able to slightly improve the shielding effect for the magnetic field and dramatically reduce the electric-field radiation (15 dBm lower).

References

[1] P. Zhao, M. Zhou, Y. Jiang, and M. Fu, "Horizontal charging area extension based on switchable relay coils," *IEEE Trans. Ind. Appl.*, vol. 58, no. 1, pp. 1071–1080, Jan. 2022.

[2] J. M. Arteaga, S. Aldhaher, G. Kkelis, C. Kwan, D. C. Yates, and P. D. Mitcheson, "Dynamic capabilities of multi-MHz inductive power transfer systems demonstrated with batteryless drones," *IEEE Trans. Power Electron.*, vol. 34, no. 6, pp. 5093–5104, Jun. 2019.

[3] P. Zhao, G. Zheng, R. He, Y. Liu, and M. Fu, "A 45-W two-stage wireless fast charger using unregulated inductive power transfer," *IEEE J. Emerg. Sel. Topics Ind. Electron.*, vol. 2, no. 3, pp. 287–296, Jul. 2021.

[4] M. R. Basar, M. Y. Ahmad, J. Cho, and F. Ibrahim, "An improved wearable resonant wireless power transfer system for biomedical capsule endoscope," *IEEE Trans. Ind. Electron.*, vol. 65, no. 10, pp. 7772–7781, Oct. 2018.

[5] S. Li and C. C. Mi, "Wireless power transfer for electric vehicle applications," *IEEE J. Emerg. Sel. Topics Power Electron.*, vol. 3, no. 1, pp. 4–17, Mar. 2015.

[6] W. Zhang, Q. Yang, Y. Li, Z. Lin, M. Yang, and M. Mi, "Comprehensive analysis of nanocrystalline ribbon cores in high-power-density wireless power transfer pads for electric vehicles," *IEEE Trans. Magn.*, vol. 58, no. 2, pp. 1–5, Feb. 2022.

[7] A. Barakat, K. Yoshitomi, and R. K. Pokharel, "Design approach for efficient wireless power transfer systems during lateral misalignment," *IEEE Trans. Microw. Theory Techn.*, vol. 66, no. 9, pp. 4170–4177, Sep. 2018.

[8] M. Fu, C. Fei, Y. Yang, Q. Li, and F. C. Lee, "A GaN-based DC–DC module for railway applications: Design consideration and high-frequency digital control," *IEEE Trans. Ind. Electron.*, vol. 67, no. 2, pp. 1638–1647, Feb. 2020.

[9] R. Ramachandran and M. Nymand, "Experimental demonstration of a 98.8% efficient isolated DC–DC GaN converter," *IEEE Trans. Ind. Electron.*, vol. 64, no. 11, pp. 9104–9113, Nov. 2017.

[10] L. A. D. Ta, N. D. Dao, and D.-C. Lee, "High-efficiency hybrid LLC resonant converter for on-board chargers of plug-in electric vehicles," *IEEE Trans. Power Electron.*, vol. 35, no. 8, pp. 8324–8334, Aug. 2020.

[11] B. Luo, D. Ma, W. Han, and J. Liu, "Extensible low-profile coplanar wireless power transfer system for multiload applications with load-independence constant current output," *IEEE Trans. Ind. Electron.*, vol. 69, no. 11, pp. 11187–11197, Nov. 2022.

[12] S. Jayalath and A. Khan, "Design, challenges, and trends of inductive power transfer couplers for electric vehicles: A review," *IEEE J. Emerg. Sel. Topics Power Electron.*, vol. 9, no. 5, pp. 6196–6218, Oct. 2021.

[13] J. Kuipers, H. Bruning, D. Yntema, S. Bakker, and H. Rijnaarts, "Self-capacitance and resistive losses of saline-water-filled inductors," *IEEE Trans. Ind. Electron.*, vol. 61, no. 5, pp. 2356–2361, May 2014.

[14] Z. Zheng, X. Fang, Y. Zheng, and H. Feng, "A wireless power transfer system based on dual-band metamaterials," *IEEE Microw. Wireless Compon. Lett.*, vol. 32, no. 6, pp. 615–618, Jun. 2022.

[15] Y.-D. Lee, K.-W. Kim, and G.-W. Moon, "A self-compensated planar coil with integrated single-switch regulator for wireless power transfer (WPT) systems," *IEEE Trans. Power Electron.*, vol. 36, no. 10, pp. 10954–10958, Oct. 2021.

[16] Z. Yi, M. Li, B. Muneer, and Q. Zhu, "High-efficiency mid-range inductive power transfer employing alternative-winding coils," *IEEE Trans. Power Electron.*, vol. 34, no. 7, pp. 6706–6721, Jul. 2019.

[17] K. Furusato, T. Imura, and Y. Hori, "Design of multi-frequency coil for capacitor-less wireless power transfer using high order self-resonance of open end coil," in *Proc. IEEE Wireless Power Transfer Conf.*, 2016, pp. 1–4.
[18] G. K. Y. Ho and B. M. H. Pong, "Multilayer flexible printed circuitry planar transformer with integrated series capacitance for an LLC converter," *IEEE Trans. Power Electron.*, vol. 34, no. 11, pp. 11139–11152, Nov. 2019.
[19] Q. Wang, M. A. Saket, A. Troy, and M. Ordonez, "A self-compensated planar coil for resonant wireless power transfer systems," *IEEE Trans. Power Electron.*, vol. 36, no. 1, pp. 674–682, Jan. 2021.
[20] R. Qin, J. Li, and D. Costinett, "A 6.6-kW high-frequency wireless power transfer system for electric vehicle charging using multilayer nonuniform self-resonant coil at MHz," *IEEE Trans. Power Electron.*, vol. 37, no. 4, pp. 4842–4856, Apr. 2022.
[21] Z. Yi, M. Li, B. Muneer, G. He, and X.-X. Yang, "Self-resonant antisymmetric planar coil for compact inductive power transfer system avoiding compensation circuits," *IEEE Trans. Power Electron.*, vol. 36, no. 5, pp. 5121–5134, May 2021.
[22] C. Jiang, D. E. Gaona, Y. Shen, H. Zhao, K. T. Chau, and T. Long, "Low-frequency medium power capacitor-free self-resonant wireless power transfer," *IEEE Trans. Ind. Electron.*, vol. 68, no. 11, pp. 10521–10533, Nov. 2021.
[23] C. M. de Miranda and S. F. Pichorim, "A self-resonant two-coil wireless power transfer system using open bifilar coils," *IEEE Trans. Circuits Syst. II, Exp. Briefs*, vol. 64, no. 6, pp. 615–619, Jun. 2017.
[24] B. Pakhaliuk, O. Husev, V. Shevchenko, K. Kroics, D. Stepins, and R. Strzelecki, "Inductive bifilar coil based wireless charging system for autonomous electric boat," in *Proc. IEEE 31st Int. Symp. Ind. Electron.*, 2022, pp. 758–761.
[25] R. Narayanamoorthi and A. V. Juliet, "Capacitor-less high-strength resonant wireless power transfer using open bifilar spiral coil," *IEEE Trans. Appl. Supercond.*, vol. 29, no. 1, pp. 1–8, Jan. 2019.
[26] K. Chen and Z. Zhao, "Analysis of the double-layer printed spiral coil for wireless power transfer," *IEEE J. Emerg. Sel. Topics Power Electron.*, vol. 1, no. 2, pp. 114–121, Jun. 2013.
[27] R. Qin, J. Li, J. Sun, and D. Costinett, "Shielding design for high-frequency wireless power transfer system for ev charging with self-resonant coils," *IEEE Trans. Power Electron.*, vol. 38, no. 6, pp. 7900–7909, Jun. 2023.
[28] S. Garcıa-Moreno and M. Bandala-Sánchez, "Fringing capacitance in sections of circular parallel plates with variable overlapping area," *IET Electron. Lett.*, vol. 49, no. 11, pp. 712–714, May 2013.
[29] N. N. Rao, *Fundamentals of Electromagnetics for Electrical and Computer Engineering*. Englewood Cliffs, NJ, USA: Prentice-Hall, 2009.
[30] *Wireless Power Transfer for Light-Duty Plug-in/Electric Vehicles and Alignment Methodology*, SAE J2954_201711, Feb. 2022.
[31] Y. Yin, H. Li, and M. Fu, "Inductive coupler analysis based on scattering parameters with nonstandard terminal impedance," *IEEE J. Emerg. Sel. Topics Ind. Electron.*, vol. 3, no. 4, pp. 1168–1176, Oct. 2022.

Yiming Yin received the B.S. degree in electronic information engineering in 2020 from ShanghaiTech University, Shanghai, China, where he is currently working toward the M.S. degree in power electronics with the School of Information Science and Technology.

In September 2019, he joined the Advanced Electric Power Conversion Laboratory, ShanghaiTech University. His recent research is the design and optimization of near-field coupler.

Heyuan Li (Graduate Student Member, IEEE) received the B.S. degree in electrical engineering from the University of Shanghai Science and Technology, Shanghai, China, in 2020. He is currently working toward the M.S. degree in power electronics with the School of Information Science and Technology, ShanghaiTech University, Shanghai, China.

His current interests include radiation model and EMI of high-frequency power converters.

Shiqi Gao is currently working toward the B.S. degree in electronic information engineering with the School of Information Science and Technology, ShanghaiTech University, Shanghai, China.

His current interests include compensation design for CPT and IPT coupler and optimization of the model structure.

Yong Li (Senior Member, IEEE) received the B.Sc. and Ph.D. degrees in electrical engineering from the School of Electrical Engineering, Southwest Jiaotong University, Chengdu, China, in 2013 and 2017, respectively.

From 2017 to 2018, he was a Research Associate with the Department of Electrical Engineering, The Hong Kong Polytechnic University, Hong Kong, and subsequently, he was a Postdoctoral Fellow with the same department. He is currently an Associate Professor with Southwest Jiaotong University, Chengdu, China. His main research interests are wireless power transfer and energy harvesting.

Dr. Li is currently a Guest Editor of Electronics for a special issue "Wireless Power Transfer and Its Applications."

Xian Zhang (Member, IEEE) received the B.S., M.S., and Ph.D. degrees in electrical engineering from the School of Electrical Engineering, Hebei University of Technology, Tianjin, China, in 2006, 2009, and 2012, respectively.

He is currently a Professor with the Hebei University of Technology, Tianjin, China. He is the team leader of State Key Laboratory of Reliability and Intelligence of Electrical Equipment, Key Laboratory of Electromagnetic Field and Electrical Apparatus Reliability of Hebei Province, Hebei University of Technology, Tianjin, China. His main research interests are wireless power transfer and engineering electromagnetic field.

Minfan Fu (Senior Member, IEEE) received the B.S., M.S., and Ph.D. degrees in electrical and computer engineering from the University of Michigan-Shanghai Jiao Tong University Joint Institute, Shanghai Jiao Tong University, Shanghai, China, in 2010, 2013, and 2016, respectively.

From 2016 to 2018, he held a Postdoctoral position with the Center for Power Electronics Systems (CPES), Virginia Polytechnic Institute and State University, Blacksburg, VA, USA. He is currently an Assistant Professor with the School of Information Science and Technology, ShanghaiTech University, Shanghai, China. He holds one U.S. patent, seven Chinese patents, and has authored or coauthored more than 80 papers in prestigious IEEE journals and conferences. His research interests include megahertz wireless power transfer, high-frequency power conversion, high-frequency magnetic design, and application of wide-bandgap devices.